Electronic Supplementary Material (ESI) for Journal of Materials Chemistry A.

Dose Rate Dependent Cation and **Anion Radiation Enhanced Diffusion in Hematite**

Kayla H. Yano, Aaron A. Kohnert, Tiffany C. Kaspar, Sandra D. Taylor, Steven R. Spurgeon, Hyosim Kim, Yongqiang Wang, Blas P. Uberuaga, and Daniel K. Schreiber

Supplemental Information

1. Further Sample Details and Irradiation Conditions

This section provides details on the sample stacks grown by MBE (Figure S1 and S2), irradiation setup and stage temperature (Figures S3 and S4), dose calculation by Stopping Range of Ions in Matter (SRIM) (Figure S5) and tabulated final irradiation values (Table S1).

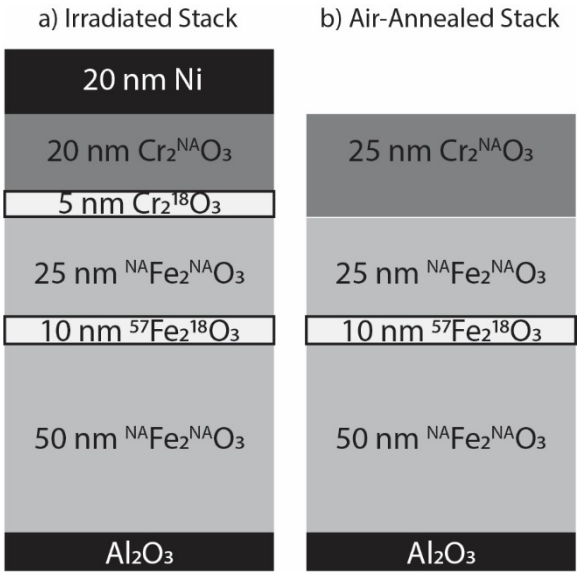

Figure S 1: Schematic illustration of the multilayer film stack designs for (a) irradiated and (b) thermally annealed films used in the current study. Isotopic species are noted as either natural abundance (NA) or enriched in the indicated isotope.

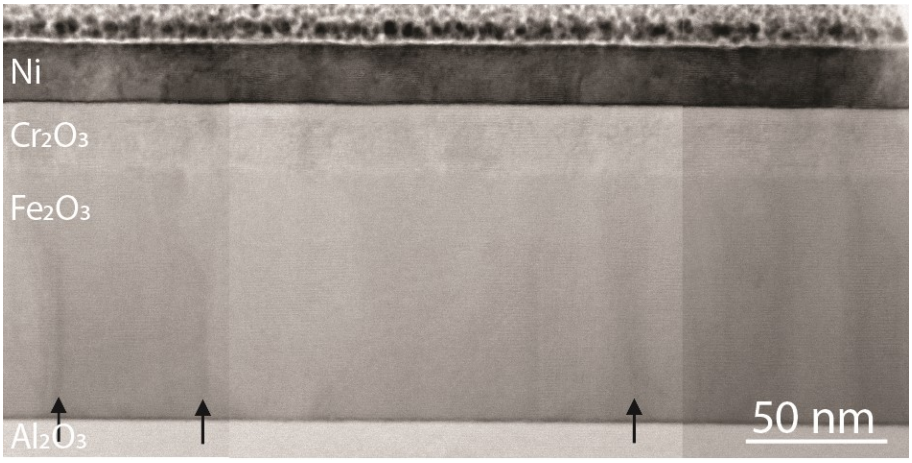

Figure S 2: Additional STEM BF imaging of as-grown MBE film. Black arrows denote vertical growth dislocations. No dislocation loops or voids are present in the Fe_2O_3 or Cr_2O_3 films.

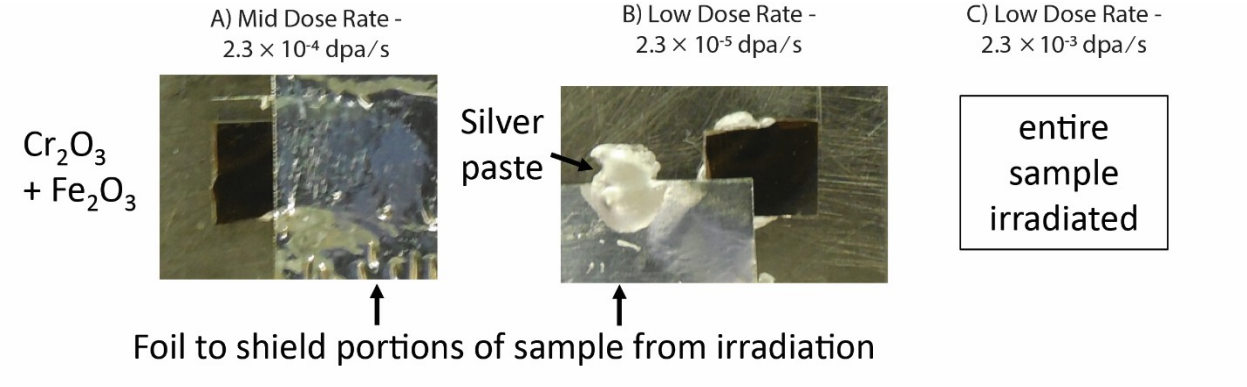

Figure S 3: Optical photographs of the ~5x5 mm^2 chips irradiated in this study. Chips irradiated at mid and low dose rates (2.3×10^{-4} and 2.3×10^{-5} dpa/s, respectively) were partially shielded with foil during irradiation. Silver paste was used to hold samples to stage.

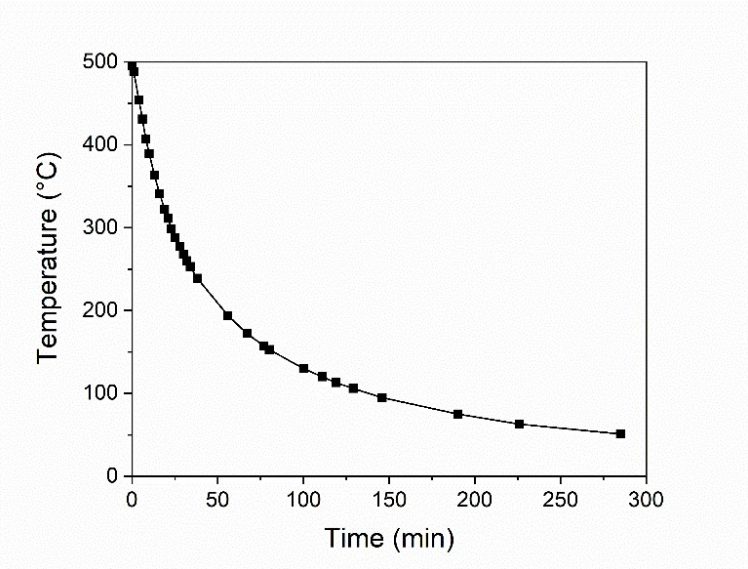

Figure S 4: Thermocouple-measured sample temperature cooling profile after irradiation at 500 °C.

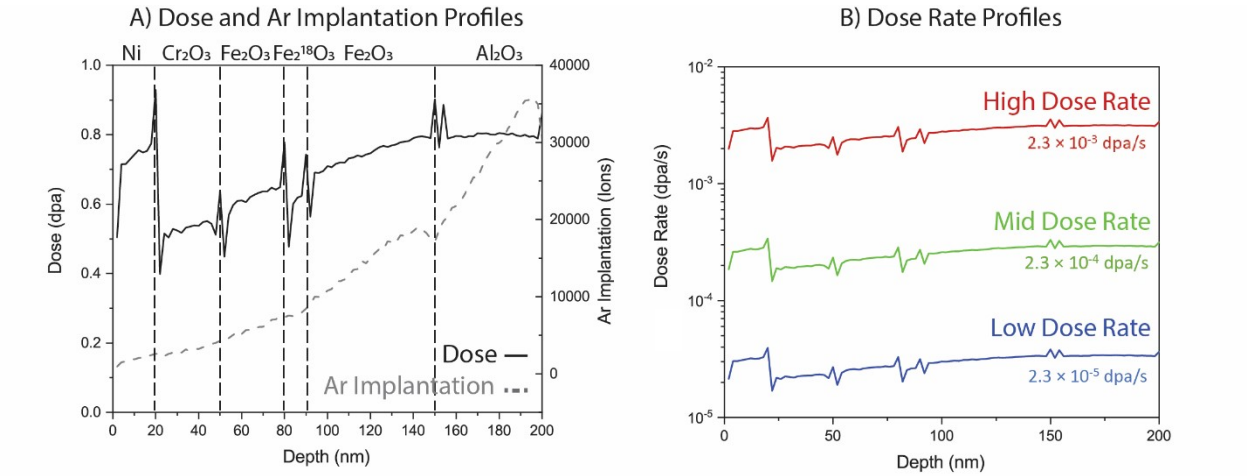

Figure S 5: SRIM[1] profiles of (A) sample dose (solid line, left axis) and Ar implantation (dashed line, right axis) as a function of sample depth based on the stack geometry shown in Fig. S1 and (B) the corresponding dose rate dependencies as a function of depth.

Table S 1: Sample irradiation parameters from this study (high, mid, and low dose rates) and from prior work using proton irradiation – ref. [2]

Name	Temperature (°C)	Irradiation Time (s)	Dose (dpa)	Ion Fluence (ions/cm²)	Dose rate (dpa/s)
High dose rate	500	254	0.6	1.15E15	2.5E-3
Mid dose rate	300	2,729			2.3E-4
Low dose rate	500	23,580			2.6E-5
Proton irradiation	450	86,400	0.1	4.65E18	1E-6

2. Supplemental APT and TEM Data

Included here are additional details and experimental results from both the APT and TEM characterization. These details are split into three sub-sections. The first is on the quantification of isotopic enrichment by APT (Figures S6-S8), the second into APT reconstruction methods (Figures S9 – S11), and finally into identification of the Fe_3O_4 phase after irradiation (Figures S12-S14).

2.1. Quantification of Isotopic Enrichment

The mass spectra for the specimens consists primarily of the ions Fe, Cr, CrO, FeO, and O (Figure S6). When evaluating the isotopic enrichment of the oxygen species, the O^{1+} peaks at 16 and 18 Da are used (Figure S7a). For the iron isotopic enrichment the Fe^{2+} peaks at 28 and 28.5 Da are used (Figures S7b). These isotope-specific O^{1+} and Fe^{2+} peaks are used to calculate the fraction of ^{18}O and ^{57}Fe as:

$$f_{18O} = \frac{N_{18O}}{N_{18O} + N_{16O}} \quad (1)$$

and

$$f_{57Fe} = \frac{N_{57Fe}}{N_{57Fe} + N_{56Fe}} \quad (2)$$

Here N_{18O} and N_{16O} represent the counts of the 16 Da and 18 Da O^{1+} peaks while N_{57Fe} and N_{56Fe} represent the 28 and 28.5 Da Fe^{2+} peaks, respectively. Fractional ^{18}O and ^{57}Fe profiles for two as-grown specimens are included in Figure S8. Uncertainty in the f_{18O} and f_{57Fe} profiles can be estimated by standard counting error (σ) as:

$$\sigma_{18O} = \sqrt{\frac{f_{18O} \times (1 - f_{18O})}{N_{16O} + N_{18O}}} \quad (3)$$

$$\sigma_{57Fe} = \sqrt{\frac{f_{57Fe} \times (1 - f_{57Fe})}{N_{57Fe} + N_{56Fe}}} \quad (4)$$

Although these uncertainties are locally dependent on the number of counts in each datapoint, typical uncertainties are ~0.02 in the profiles provided here and never exceed 0.05 in the presented data.

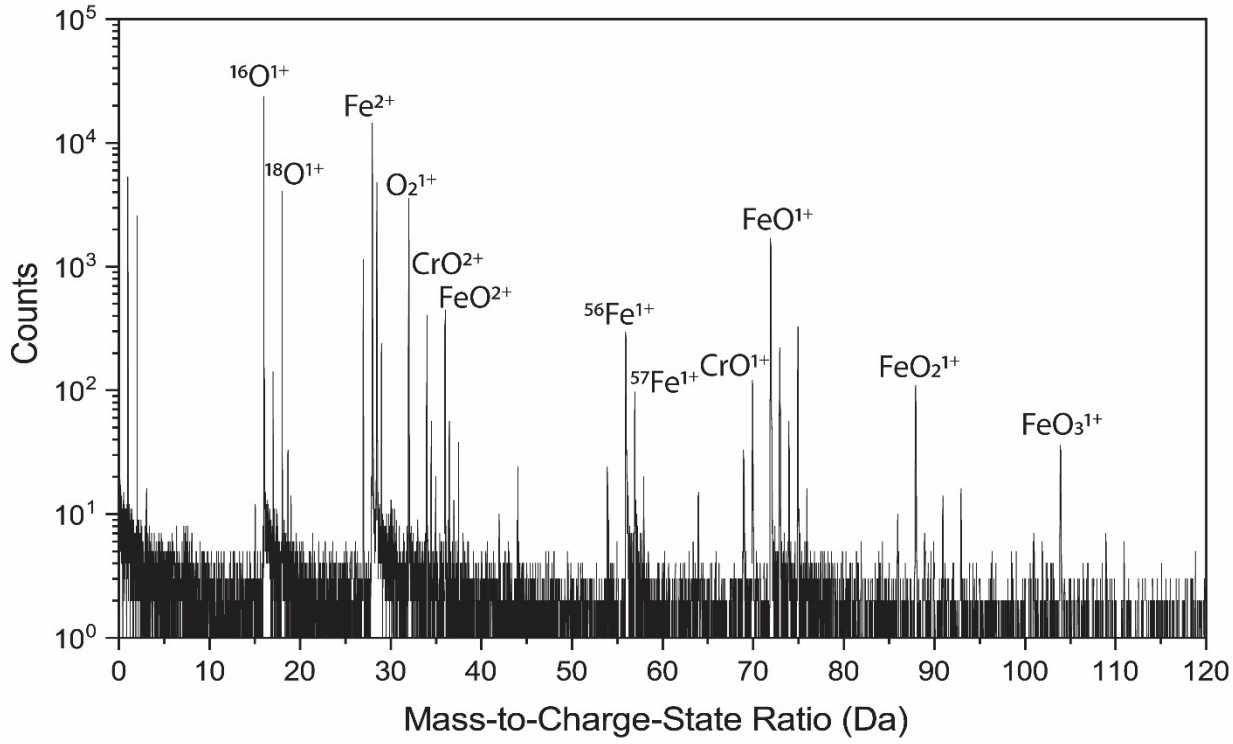

Figure S 6: Representative APT mass spectrum, taken from an as-grown film stack with most major peaks labeled.

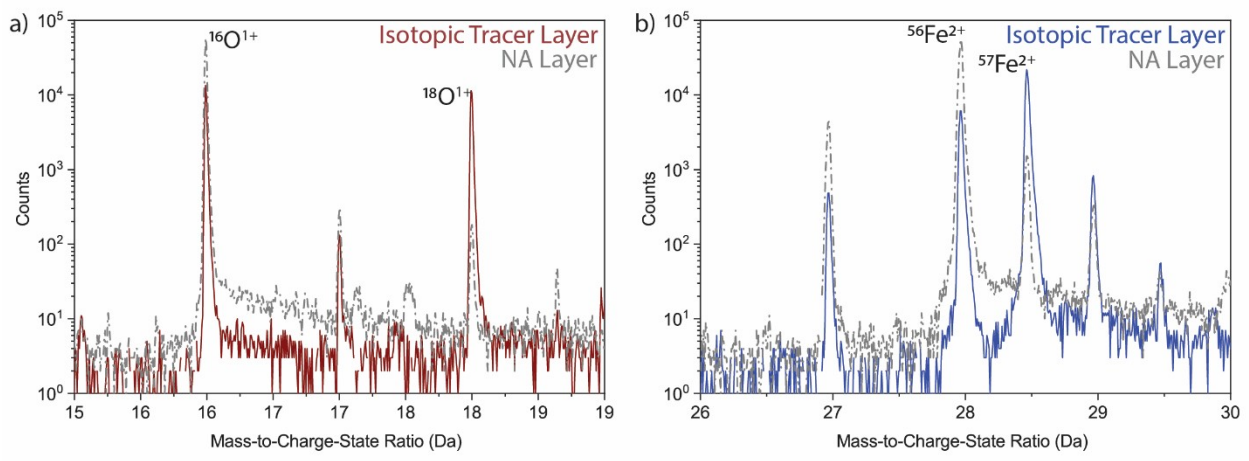

Figure S 7: Closer inspection of APT mass spectrum regions used for quantifying the local isotopic enrichment for O and Fe, specifically from the O1+ and Fe2+ peaks. Dashed lines represent natural abundance (NA) regions of the sample, and the solid lines from regions enrichment in ^{18}O and ^{57}Fe.

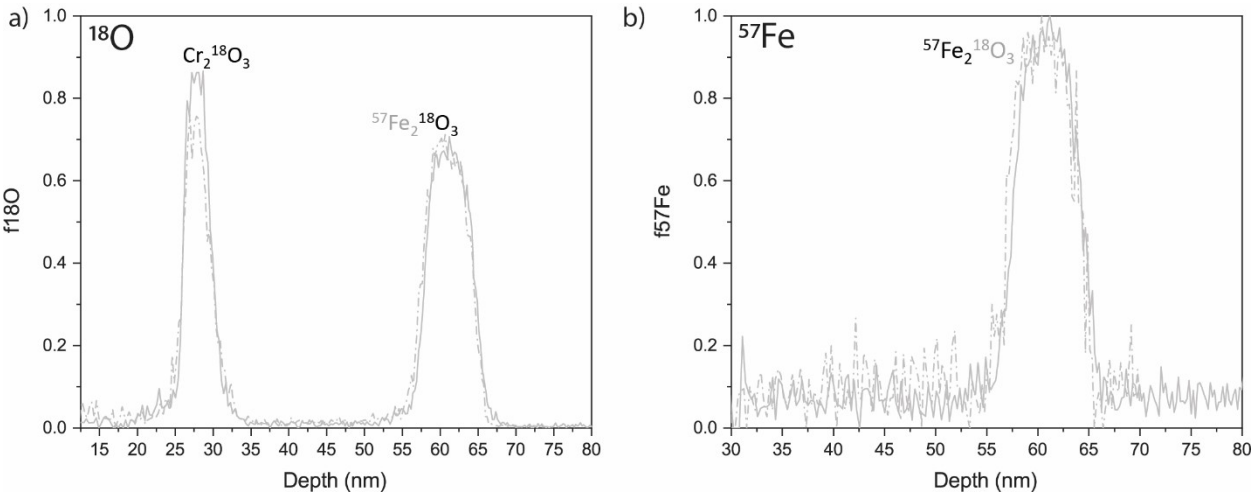

Figure S 8: APT measurements of the f_{18O} and f_{57Fe} profiles from two as-grown APT specimens demonstrating good reproducibility of both the isotopic enrichment profiles and spatial scaling of the reconstructions.

2.2. Scaling of APT reconstructions and effect of assumed resolution limits

The bilayer spacings of Fe_2O_3 and Fe_3O_4 (2.3Å and 4.8 Å – Figure S9) are used to scale the APT reconstructions accurately based on the observable spatial distribution map (SDM) (Figure S10). Combining these interplanar spacings with our previously discussed isotopic fraction uncertainty (σ<0.05), we can visualize how an idealized APT measurement of different characteristic diffusion distances and corresponding diffusion profiles appear. This is presented in Figure S11, where each profile represents the error function solution to Fick's 2nd law using D and t values to reproduce characteristic diffusion distances ($l = \sqrt{4Dt}$) from 0.3 nm to 1 nm. From these plots, it is clear that l = 0.5 nm is readily observable, and 0.3 nm is likely near the resolution limits of the technique. This relationship between D, t, and assumed resolution limits are visualized in Fig. S11 for a few assumed resolution limits, defining zones where APT can be expected to resolve diffusion or any diffusion may be undetected. In general, we view that l = 0.5 nm is a reasonably conservative estimate of our detection

limits, and more rigorous statistical analyses may extend this further. Our experimental measurements are plotted against these curves, and the time scale has been extended out to waste form relevant values (100 yrs or 3×10^9 sec). Even with APT's exceptional spatial resolution, the previously noted Arrhenius extrapolation of O diffusion in Fe_2O_3 to 300C (~10^{-45} m^2/s) is 14 orders of magnitude away from the detection limit after 100 years of annealing. On the other hand, at times of 5 minutes the minimum diffusivity resolvable is 2×10^{-22} m^2/s. It can therefore be challenging to balance the extremes of experimental detectability, practical laboratory time scales, relevant diffusivity values, and even dose rates and cumulative dose (i.e. 10^{-3} dpa/s in minutes vs 10^{-5} dpa/s in hours vs 10^{-13} dpa/s in hundreds of yrs). However, it is also worth emphasizing that APT's resolution and detection limits provide new opportunities for nanoscale mass transport that were previously impossible by other techniques that required micrometers of diffusion for reliable quantification.

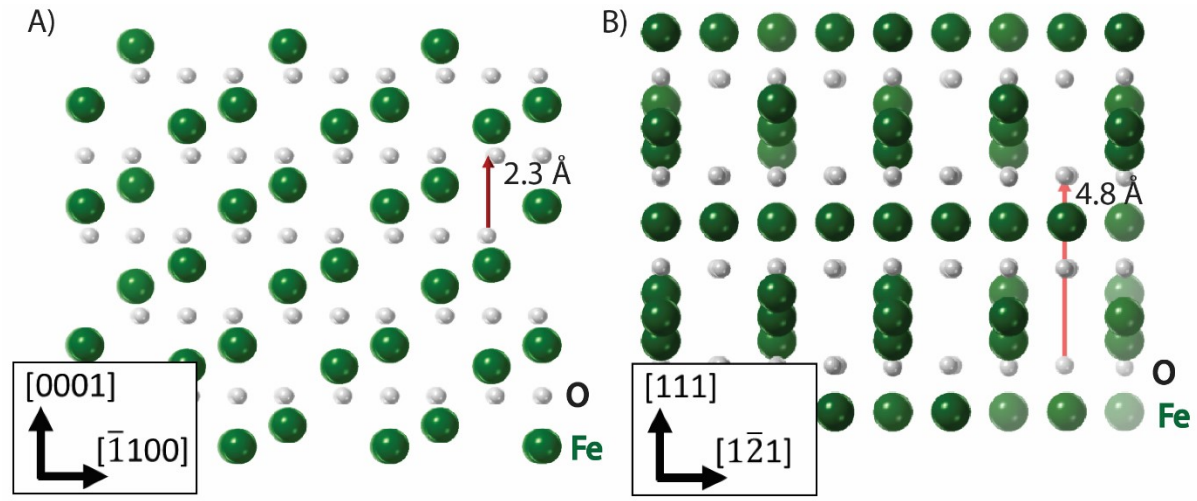

Figure S 9: Ball and stick models of (A) Fe_2O_3 and (B) Fe_3O_4 with the indicated [0001] (Fe_2O_3) / [111] (Fe_3O_4) O bilayer spacing.

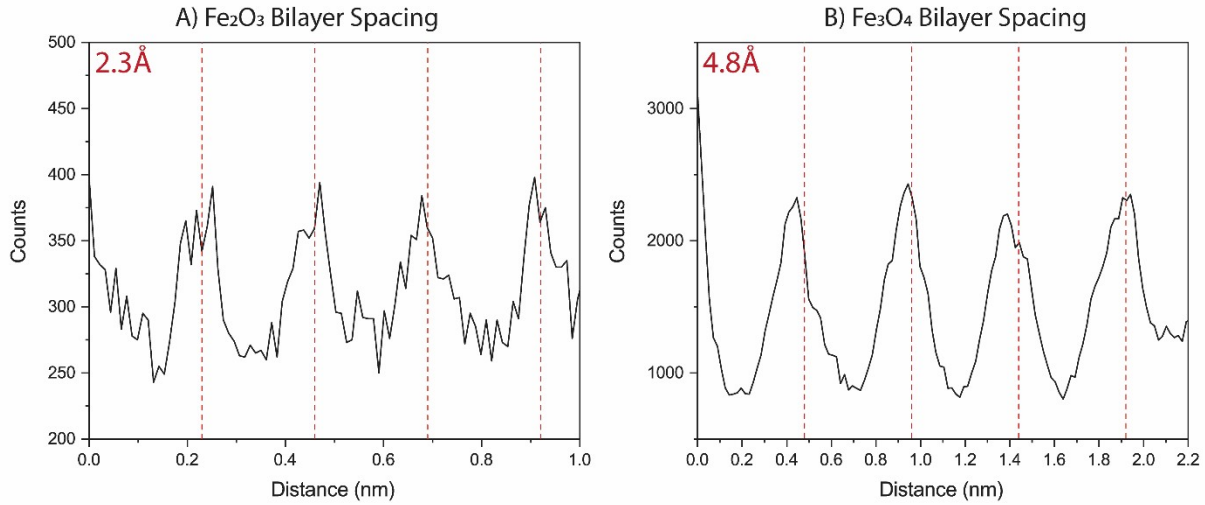

Figure S 10: APT derived spatial distribution maps (SDMs) of interplanar spacing along the Z-axis used for scaling of the APT reconstruction in (a) Fe_2O_3 and (b) Fe_3O_4. The red dashed lines indicate the true O bilayer spacing expected in the data versus the experimentally measured SDM (black lines).

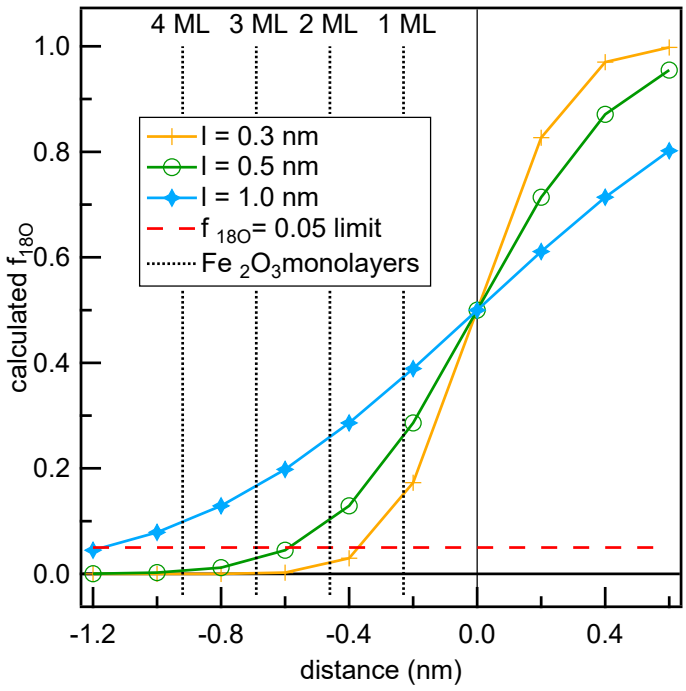

Figure S 11: Representative calculated diffusion curves for characteristic diffusion distances of 0.3 nm, 0.5 nm, and 1.0 nm. The curves are sampled at 0.2 nm spacings, as would be done in the APT measurement. Vertical and horizontal lines indicate 0.23 nm interplanar spacings of Fe2O3, and the f18O = 0.05 uncertainty limit from counting statistics, respectively. These plots show that at the l = 0.5 nm resolution limit (D_{limit}) approximately ~5-7 APT data points are within counting error limits, or ~5 monolayers of interdiffusion.

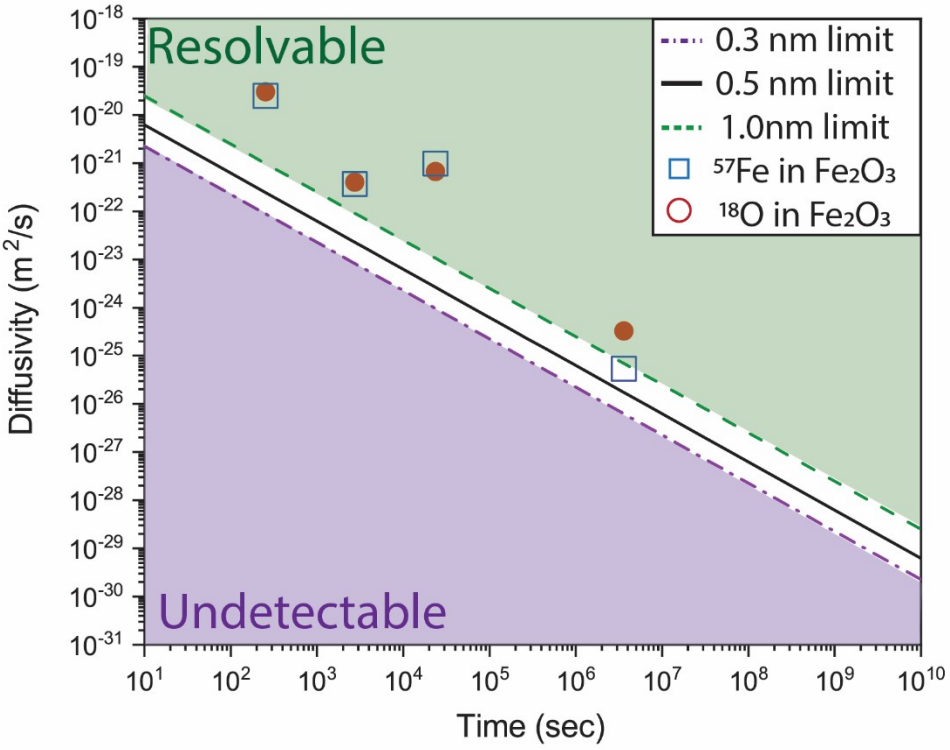

Figure S 12: Resolution limit of the APT and isotopic tracer technique. Limits of 0.3 nm, 0.5 nm, and 1 nm are provided to give an idea of the range of D values based on more (1nm) or less (0.3 nm) conservative estimates of the resolution limit. Experimental D values are included for context.

2.3. Identification and impact of localized Fe_2O_3 reduction to Fe_3O_4

Regions of the Fe_2O_3 near the Cr_2O_3 interface reduced to Fe_3O_4 and this transformation was captured by TEM (Figure S13) and APT (Figures S14 and S15) in both low and high dose rate samples (500°C) but not in the mid dose rate sample (300°C). The depth of Fe_3O_4 reduction varied across the samples reaching at most (in the regions captured by TEM) 40 nm from the Cr_2O_3 interface. In regions where the Fe_3O_4 transformation reached the isotopic tracer layer, the ^{57}Fe tracer rapidly diffused through the reduced volume, while the ^{18}O did not (Figure S15). This phenomenon will be the subject of a future paper.

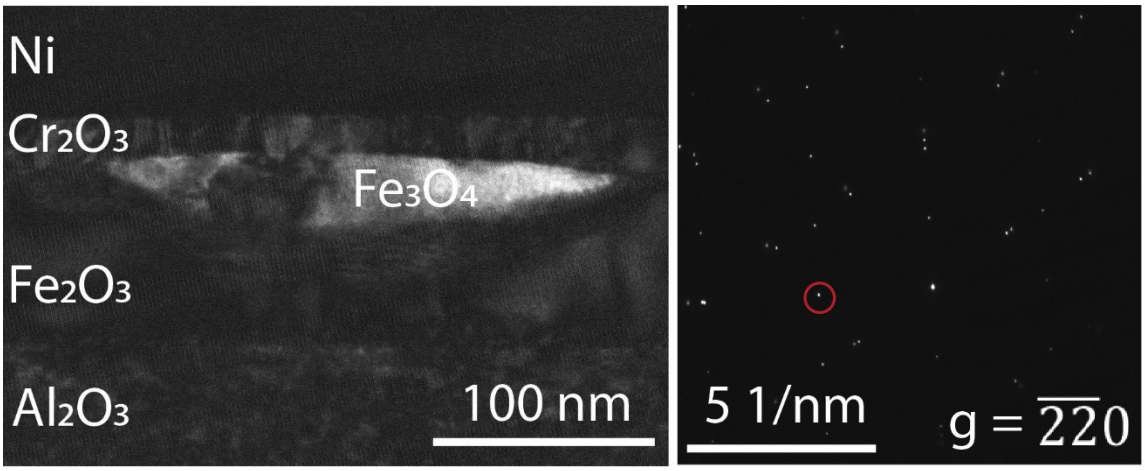

Figure S 13: Darkfield TEM image and corresponding diffraction pattern to visualize the extent of Fe_3O_4 formation in high dose rate sample. The observed Fe_3O_4 region is directly beneath the Cr_2O_3 film, extending at most (in this region) 40 nm into the Fe_2O_3 film.

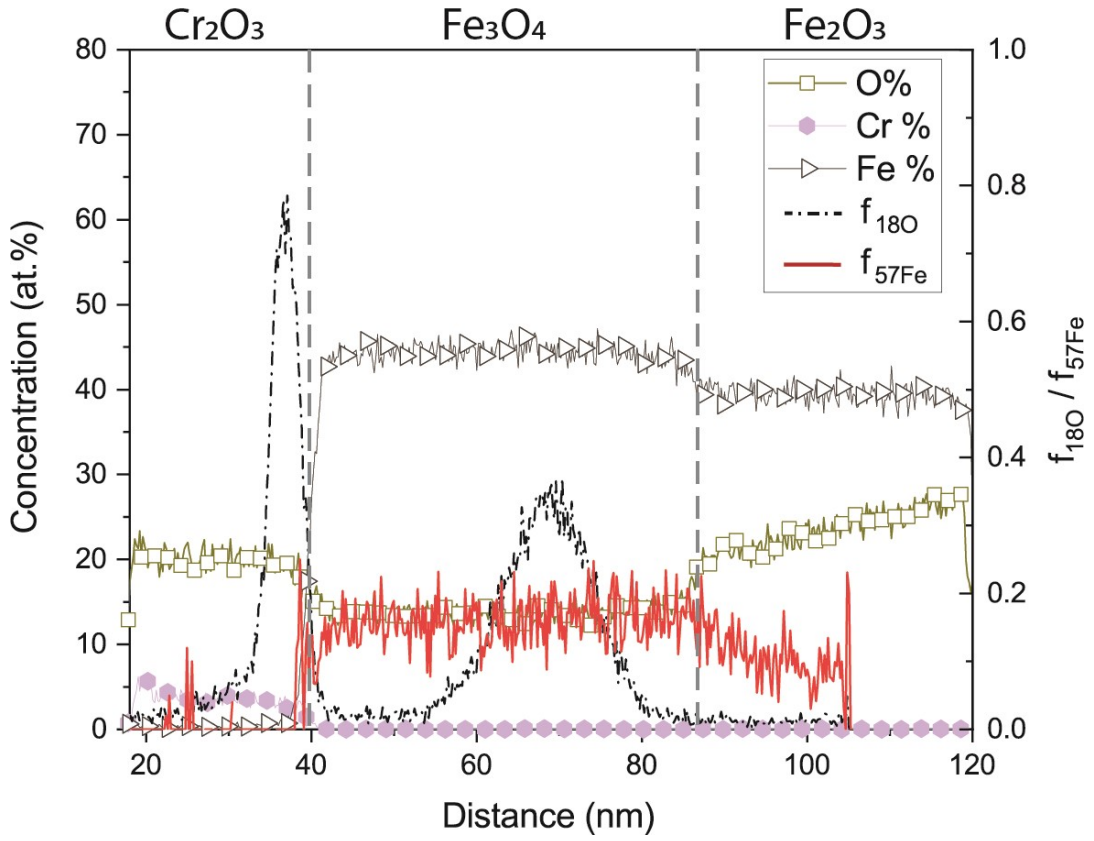

Figure S 14: APT-measured mixed atomic and isotopic concentration profiles across a film stack in which the irradiated Fe_2O_3 has partially transformed to Fe_3O_4. While the ^{18}O tracer remains relatively in-place, the ^{57}Fe is seen to rapidly diffuse throughout the transformed Fe oxide.

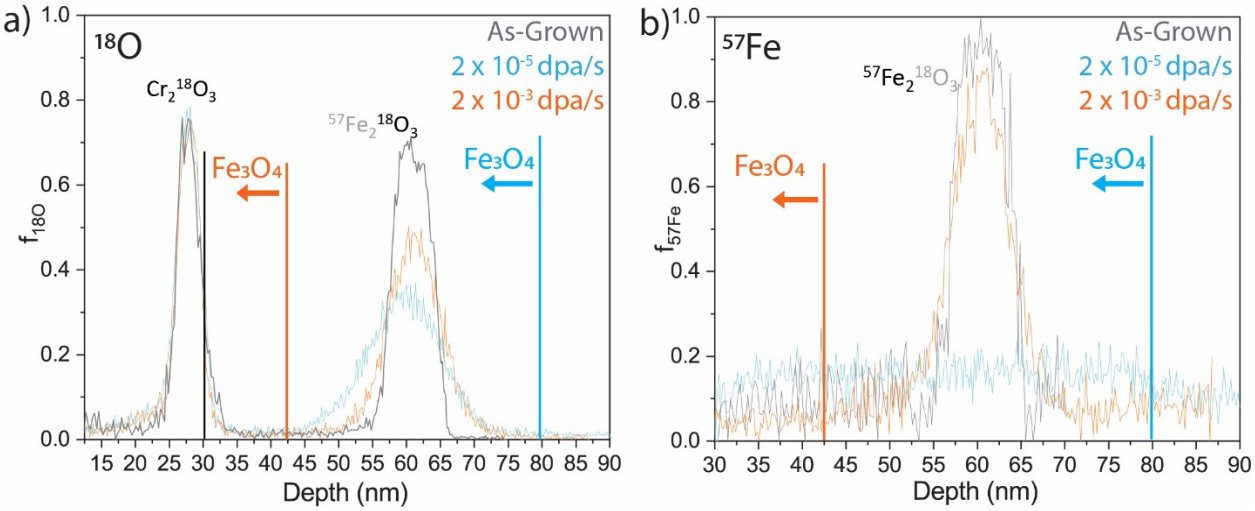

Figure S 15: APT-measured f_{18O} and f_{57Fe} profiles of irradiated and as-grown samples. An APT specimen from the high dose rate irradiation exhibits partial Fe_2O_3 → Fe_3O_4 transformation to the indicated positions (orange). When the transformation has not yet reached the tracer layer, the transformation seems to have no perceived effect on the tracers. Conversely, when the conversion reaches the tracer layer (as in a specimen from the low dose rate irradiation – blue), the ^{57}Fe cation distributes throughout the transformed region and ^{18}O does not.

3. References

1 J. F. Ziegler, 2013.

2 K. H. Yano, A. A. Kohnert, A. Banerjee, D. J. Edwards, E. F. Holby, T. C. Kaspar, H. Kim, T. G. Lach, S. D. Taylor, Y. Wang, B. P. Uberuaga and D. K. Schreiber, *Chem. Mater.*, 2021, **33**, 2307–2318.